Test Results and Alternate Packaging

Of a Damped Piezoresistive MEMS Accelerometer

Test Results and Alternate Packaging of a Damped Piezoresistive MEMS Accelerometer

Abstract

A new piezoresistive (PR) silicon accelerometer, manufactured with micro-electromechanical systems (MEMS) technology, has been developed for use with fuzing, pyroshock and other hostile environment applications. The MEMS device incorporates stops and squeeze film damping to reduce damage from over travel and resonant amplification ("Q") that may occur during violent events. Damping of the 20kG full scale device is slight to reduce Q yet create minimal phase delay. The PR bridge has relatively high input resistance (5kΩ) for low power consumption and self-heating. This paper presents recent test results of the new sensor and introduces alternate choices of packaging. The conventional metal case with mounting screws can be replaced by ceramic surface mount package, chip-and-wire hybrid packaging or flip chip configuration to minimize its circuit footprint. Test results and discussion is provided on the tradeoffs of these packaging choices.

Introduction

Evaluation testing has begun on a family of piezoresistive shock accelerometers for extreme shock applications. For this family a unique 20kG silicon MEMS sensor was developed incorporating stops and damping. Discussed in this paper are several sets of results: one with a Hopkinson bar, two with gun-launched penetration, and two metal-on-metal hammer tests, all of which confirm the beneficial effect of damping in shock environments. Tests were performed side-by-side with legacy MEMS devices (used since the 1980's), that are undamped, unstopped, and have high resonance frequencies. The tests compared the sensors and the packaging in which they were housed.

For most tests the new device was housed in an untraditional titanium package matching the size and two-hole pattern of the traditional flat steel package of the legacy sensor. However, in a side-by-side test described below, the data from the new sensor in the hard-mounted package is compared to the legacy sensor in a much larger mechanically filtered package, both subjected to metal-to-metal hammer conditions.

One of the hammer tests was performed with both sensors in their respective ceramic leadless chip carrier (LCC) packages which were surface mounted to a circuit board. This packaging alternative reduces the footprint by 80% from the original metal package. As a further reduction, since the new sensor is hermetic, with some modification it can be a package by itself. Modifications of the MEMS element to a "flip-chip" configuration allow solder connections to a circuit board through solder balls on the sensor itself. The footprint of the flip-chipped sensor would be an additional 80% reduction from the surface mount package, or more than a factor of 20 from the original metal package size.

As will be discussed later, a triaxial surface mount block for the flip chip sensor will result in similar miniaturization compared to conventional triaxial configurations.

Review of the Sensor

Past designs of MEMS shock sensors emphasized extremely high resonance frequencies. As a result, the small displacement of the inertial mass, along with the use of single crystal silicon, resulted in very low damping and correspondingly extreme values of resonant amplification. Users of past designs were forced to choose less sensitive higher range sensors and in some cases mechanical isolation to avoid electrical saturation and sensor over-range failures during shock events. Stops and squeeze film damping were incorporated in the new sensor to avoid this weakness [1]. A lower resonance frequency was necessary, using a more flexible spring-mass system so displacements were large enough (measured in microns rather than nanometers) that dimensional control could be sufficiently precise to limit travel, prevent damaging stress, regulate air flow and thus control energy dissipation. By design the frequency chosen also satisfied the bandwidth requirements of fuzing and pyroshock.

The new sensor is a hermetically sealed sandwich of three silicon layers, Base, Core and Lid, depicted in Figure 1. The middle Core layer holds the “X” shaped mass with four cantilevers, two on its top surface and two below, constraining the mass to planar motion and assuring extremely low transverse sensitivity. The direction of sensitivity is normal to the mounting surface. The Lid and Base layers provide mechanical stops to protect against over-travel of the mass, and grooves in the Lid and Base control the flow of squeezed air and therefore degree of damping.

Expanding the family to a planned higher-range 60kG version will simply require thicker cantilevers. This will use the same advanced semiconductor processes now employed for the 20kG range, which give the advantages of precise control of dimensions and parameters.

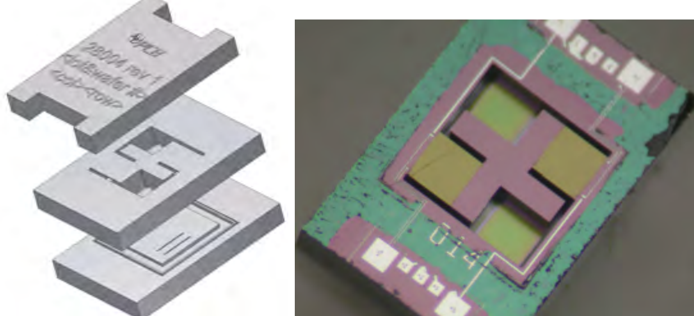

Figure 1. Exploded view of sensor, and a photograph of a core layer extracted from the sandwich. The glass frit used to bond the Base to the Core and the Core to the Lid is the teal-colored residue around the periphery of central area. The four larger aluminum pads are the wirebond pads, and the smaller pads allow in-process trimming of the Zero Measurand Output (ZMO).

For all ranges, the semiconductor strain gauges are implanted into the top surface of the Core, at locations closest to the rim and the mass for “tension” and “compression” gauges, respectively, in a conventional Wheatstone bridge. The design of the structure

and gauges resulted in a Full Scale differential output of the Wheatstone bridge of 2% of the excitation voltage.

Another process used for improved control is the boron implantation, which benefits several performance parameters dealing with the bias error of this dc coupled device. With fully active Wheatstone bridges, the cause of ZMO (or bias) is the degree of mismatching of resistance value of the tension and compression gauges, and Thermal Zero Shift (TZS) is the difference of how the two sets of gauges change over temperature, both of which are a function of the concentration of boron. Uniformity of concentration thus reduces both ZMO and TZS.

The tension and compression gauges on the legacy sensor are on opposite faces of the wafer, so are created by two distinct doping operations. It is more difficult to match opposite sides than devices on the same side of a wafer. The effect of this was demonstrated with warmup tests of both new and legacy sensors in LCCs on a fiberglass circuit board. In a private communication, the new sensor's warmup drift was more than 4 times smaller than that of the legacy sensor.

The performance of the 20kG sensor is listed in Table I, shown alongside the 20kG version of the legacy sensor to which it is compared in the tests discussed later.

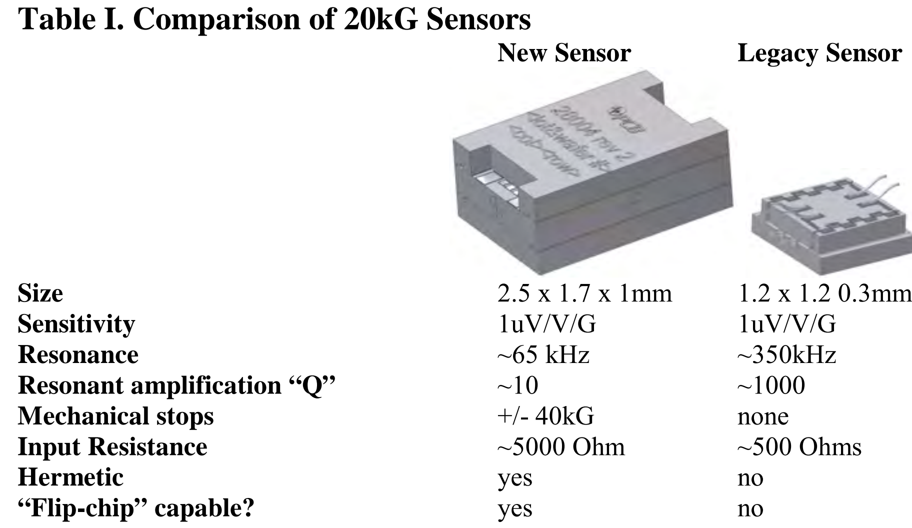

Table I. Comparison of 20kG Sensors

	New Sensor	**Legacy Sensor**
Size	2.5 x 1.7 x 1mm	1.2 x 1.2 0.3mm
Sensitivity	1uV/V/G	1uV/V/G
Resonance	~65 kHz	~350kHz
Resonant amplification "Q"	~10	~1000
Mechanical stops	+/- 40kG	none
Input Resistance	~5000 Ohm	~500 Ohms
Hermetic	yes	no
"Flip-chip" capable?	yes	no

Review of Current Packaging

Figure 2 shows the three current package configurations, all used with the same MEMS sensor. The most common is the conventionally shaped metal package, yet it conceals unconventional design features: the case is low mass, made of titanium, and in the cable all conductors are made of silver coated Kevlar fibers. Pull strength is improved, and mass is reduced compared to the conventional copper conductors. Insulators are noise-treated to reduce triboelectric noise.

Figure 2. Scaled comparison of packaging configurations, shown approximately twice actual size. Above is the metal case with its cable, below that is the flip chip sensor and the substrate subassembly that can be used in hybrid chip and wire applications, and at bottom is the surface mount ceramic leadless chip carrier. Fixturing and techniques exist for determining sensitivity of all configurations.

Packaging affects performance. The lighter titanium can be more securely constrained by mounting screws than heavier stainless. One potential impact of using titanium is that thermal conductivity of titanium is poorer than stainless steel. This lengthens the time to come to thermal equilibrium, which is one aspect of warm-up drift. However, the new sensor's input resistance is an order or magnitude higher. This means the power which needs to be dissipated through the package (or drawn from batteries) is an order of magnitude lower, so the thermal step that must be attained at equilibrium (and any zero shift associated with that temperature change) is ten times smaller.

Testing

Environmental tests were performed initially at the manufacturer in New York, described in Reference [1], but the tests generally had energy too small to adequately simulate harsh field environments. The following tests were performed at outside facilities with greater testing capabilities.

Hopkinson Bar Tests

The first tests described were performed on a Hopkinson bar with the capability for pulse shaping as well as use of a quartz disk used as a force reference, from which acceleration could be calculated. As shown in Figure 3, the test was performed as a side-by-side comparison with either 20kG and 60kG versions of the legacy sensor. Results of testing at 10kG and 40kG are shown in Figures 4 and 5.

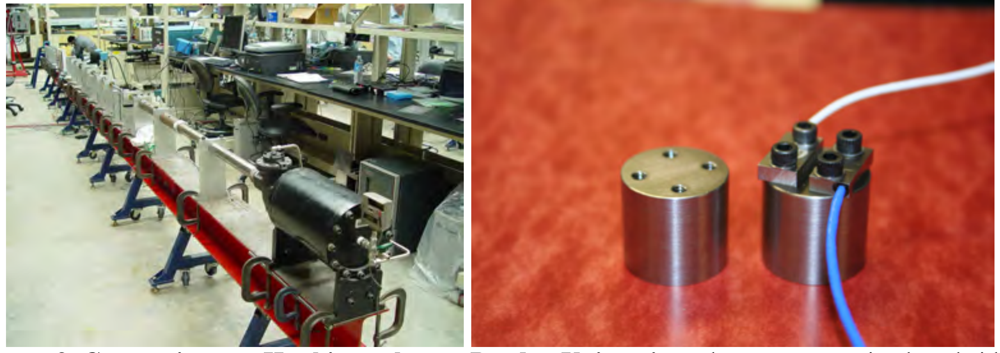

Figure 3. Comparison on Hopkinson bar at Purdue University. The new sensor is placed side-by-side with the legacy sensor on a tungsten flyaway. Photos and data shown in following graphs are courtesy D. Frew and H. Duong of Sandia National Laboratory. [2]

The quartz disk was placed between the end of the bar and the flyaway. The output of the quartz force gauge was scaled by the total mass of the flyaway and sensors as an independent measure of acceleration. That value was overlaid in the graphs, to be compared to that measured by the accelerometers.

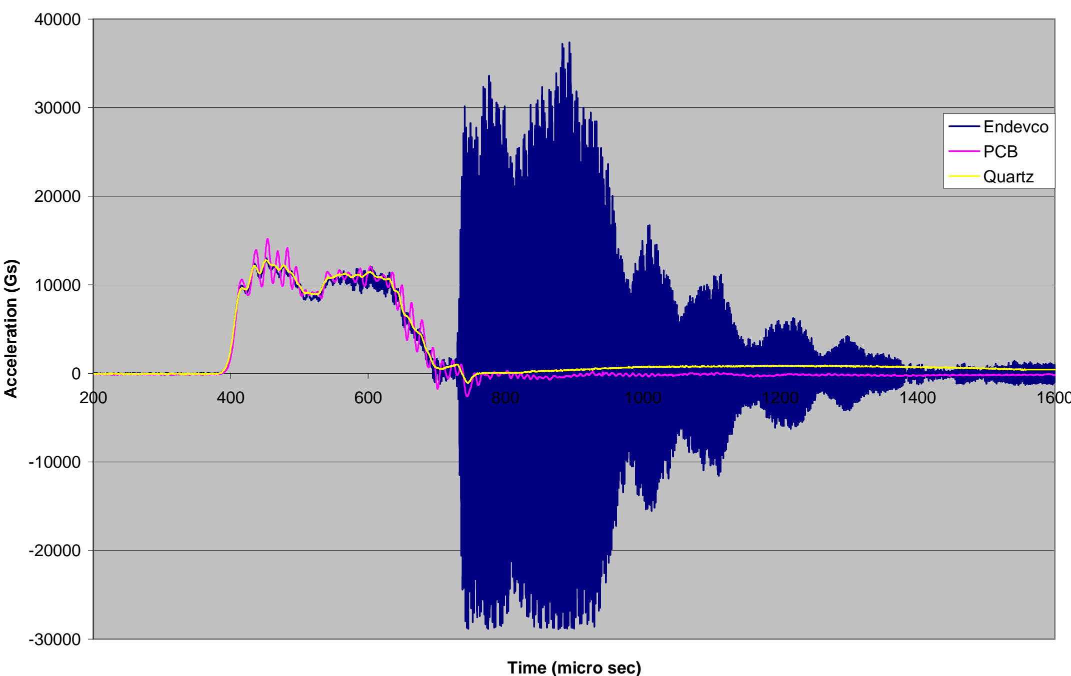

Figure 4. Comparison at 10kG. Low level tests showed good correlation of three sensors. The new sensor showed some low Q resonant amplification during the initial pulse, and the legacy sensor (20kG) showed extremely high Q response after the flyaway fixture detached from the bar. After flyaway separation, some zero shift is observed on the output of the piezoelectric quartz disk.

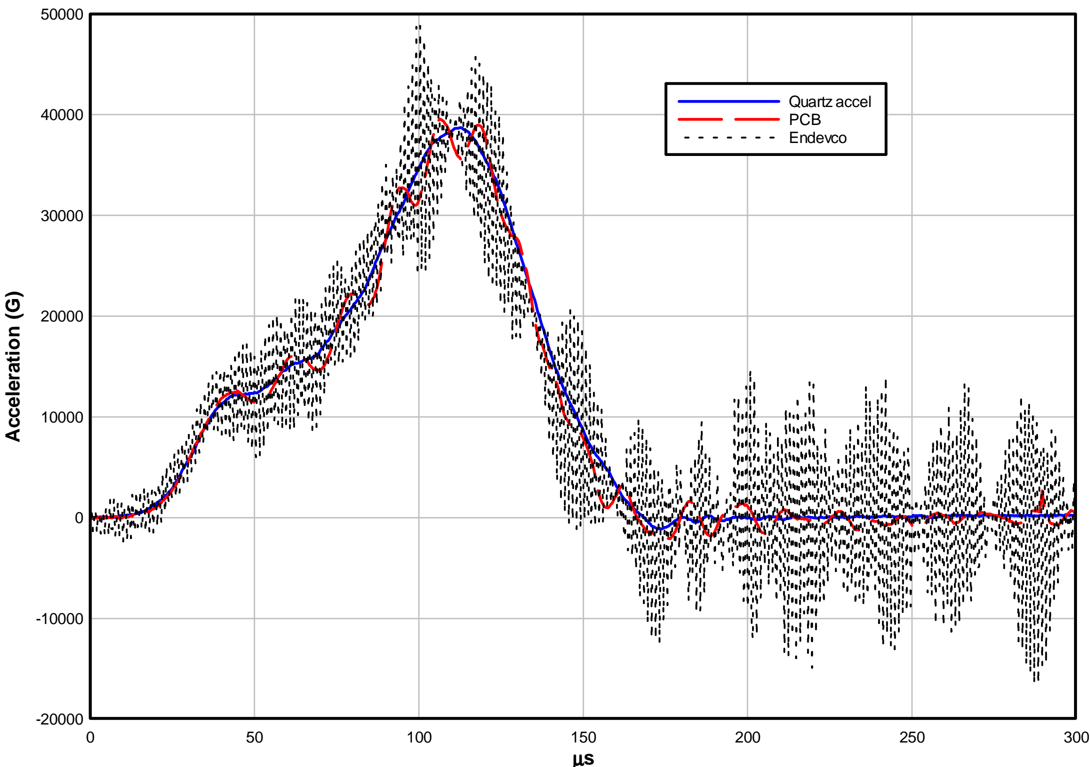

Figure 5. Comparison at 40kG. Wideband data shows ~40kG amplitude was still below stop levels of the new sensor, and linearity was apparently good at twice Full Scale. High Q response of legacy sensor (60kG) is visible throughout the pulse.

An additional test, not shown, with only the new sensor at >200kG, resulted in a broken sensor. Analysis of the surprisingly limited damage is shown later.

Penetration Tests

The drawings of Figure 6 depict the ~100 pound STUBBI penetrator and canister which was launched at ~850ft/s through a 2 foot thick concrete target at Eglin AFB in Ft. Walton Beach, Florida. The sensor was mounted in the canister alongside the 60kG legacy sensor with the batteries and recorders, which stored the entire event of set-back, penetration and final stoppage in the embankment behind the target. The penetration data is presented in Figure 7. Preliminary analysis of the new sensor output gave reasonable set-back and velocity changes, with no indication of zero shifts. All sensors survived the event, but unfortunately a wire failure in the accompanying legacy sensor's circuit prevented comparison data.

Figure 6. Configuration for test in STUBBI Penetrator. Two sensors were mounted in an instrumentation canister, along with batteries and recorders packed in glass beads. The recorders were set to 1MHz sample rate and 125kHz antialiasing filter. Illustration courtesy of A. Beliveau of Eglin AFB AFRL.

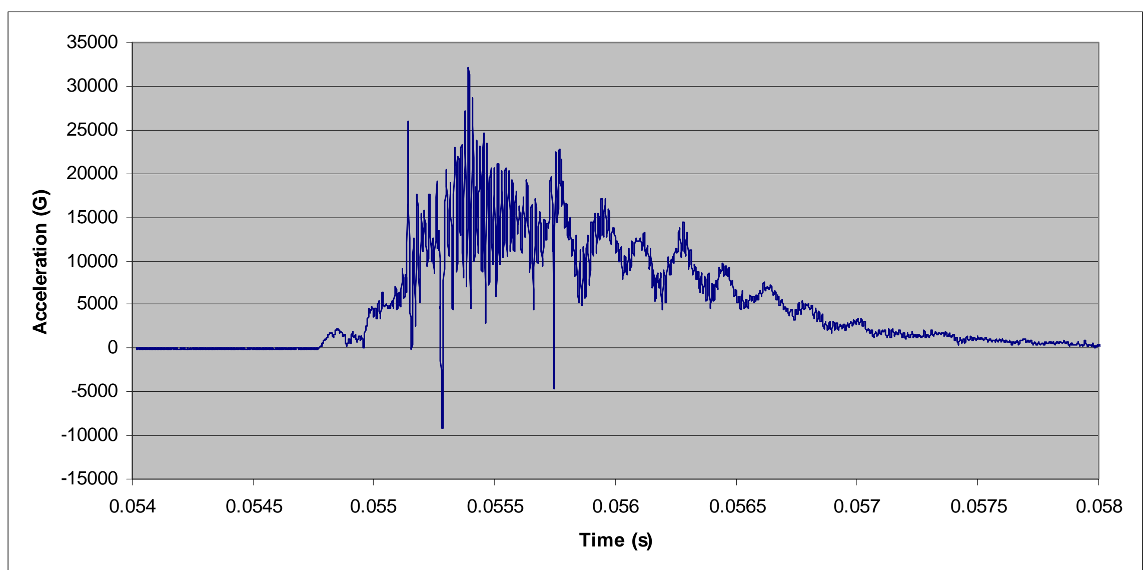

Figure 7. Waveform while penetrating 2 ft concrete. The new sensor's ~65kHz resonance damped quickly to show both the rigid body deceleration causing ΔV of ~750 ft/s during impact and the structural modes of the STUBBI penetrator and instrumentation canister. Data courtesy of J. Foley and A. Beliveau of Eglin AFB AFRL.

Another penetration test was performed at the US Army ERDC, Vicksburg MS. Two recorders were used with three channels each, sampling at 75kH with 10kHz filters the outputs of triaxial arrangements of the new and legacy sensors. They were launched at ~1440 ft/s into unreinforced unconfined 6000 psi concrete, stopping within the concrete after 33" of penetration and a peak deceleration of 15kG. The physical configuration is shown in Figure 8 and data in Figure 9.

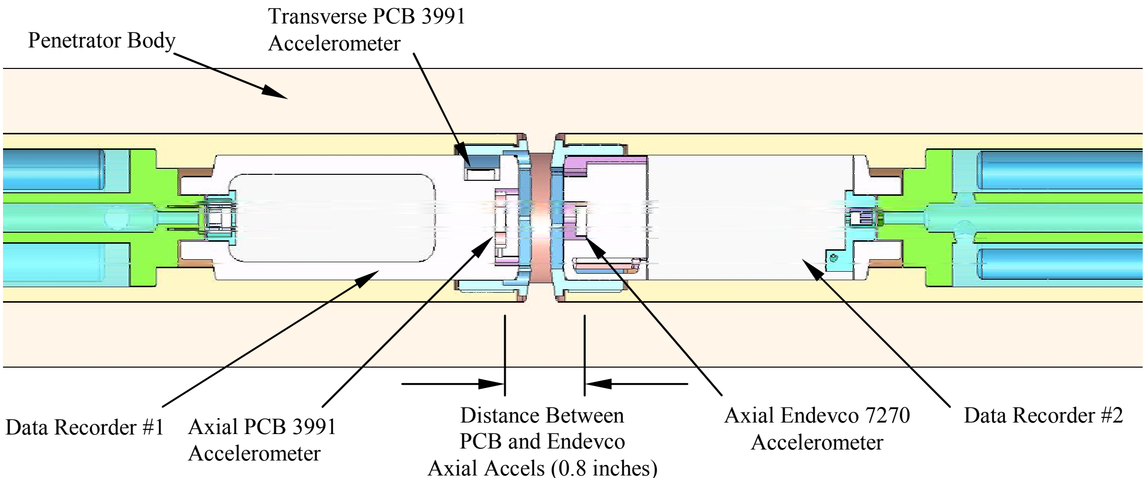

Figure 8. Placement of sensors and recorders. The front of the 3” diameter 30 lb penetrator is at the left. The sensors were closely spaced by the back-to-back arrangement of the canisters so the accelerations would be well correlated. Illustration courtesy of D. Frew, Sandia National Laboratory.

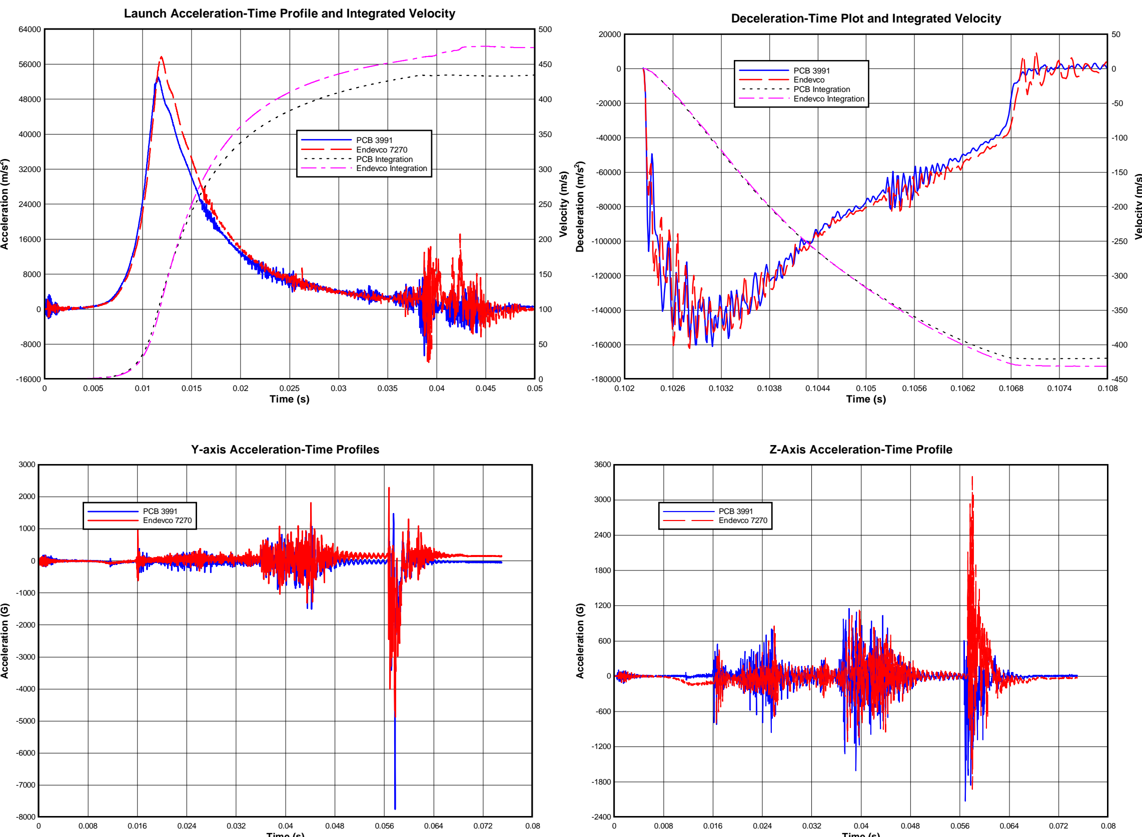

Figure 9. Comparative waveforms of triaxial sensors. Waveforms at upper left and right represent the sensors during launch and impact, respectively, each oriented in the axial direction. The transverse data for the launch are the lower graphs, showing the largest rattle when leaving the barrel. Both legacy sensors in the transverse directions display zero shift. Data is courtesy of R. Hastie, US Army ERDC, Vicksburg MS.

Hammer Tests

Two sets of hammer tests were performed, covering a variety of packaging. In the first set, sensors in side-by-side LCCs surface-mounted to a fiberglass circuit board were powered and operated while on a “VHG” shock machine at its maximum setting of ~90kG. Tests were performed at various temperatures, as low as -54C. Although no data was released, both sensors were reported to survive, with anecdotal observation that resonances were stronger when cold. (This is supported theoretically, since viscosity of the trapped gas in the new sensor would decrease by ~20% at that temperature.)

Another metal-on-metal hammer test was performed, depicted in Figure 10, side-by-side with one each of 20kG and 60kG versions of the legacy sensor. The new sensor was hard mounted to the test specimen, whereas the legacy sensors were configured in a mechanically filtered housing.

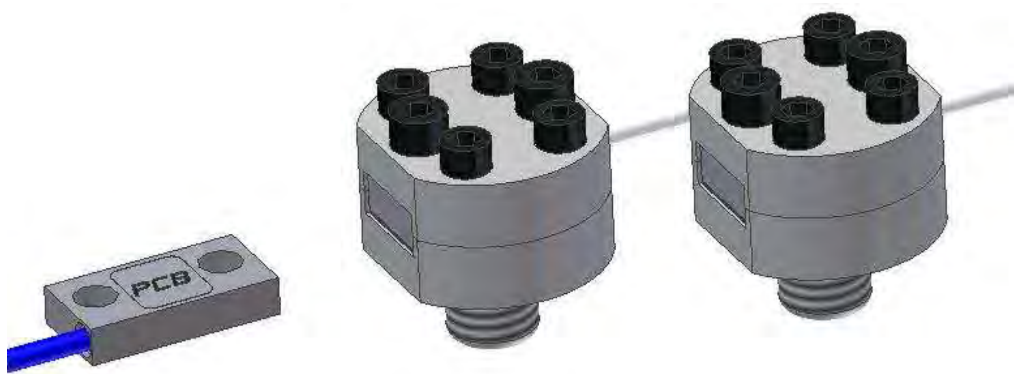

Figure 10. Orientation for hammer tests. This depiction shows the size and approximate separation of the new sensor alongside mechanically-filtered legacy sensors on the test specimen, which is not shown. Point of impact was near the sensors, in a direction normal to the mounting surface, and therefore parallel to the sensitive axis of all sensors. The mechanically filtered package is traditionally used to prevent failure due to Over Range from resonant amplification of high Q legacy sensor during explosive events and metal-to-metal impacts.

The hammer test consisted of approximately 100 blows in rapid succession, with each blow generating peaks at approximately 10kG as measured by the wideband data acquisition (5MHz sampling with 2.5MHz antialias filters). Data is shown in Figures 11-12. Despite the mechanical filtration, the legacy sensors showed considerable high frequency input and their resonance frequencies were excited.

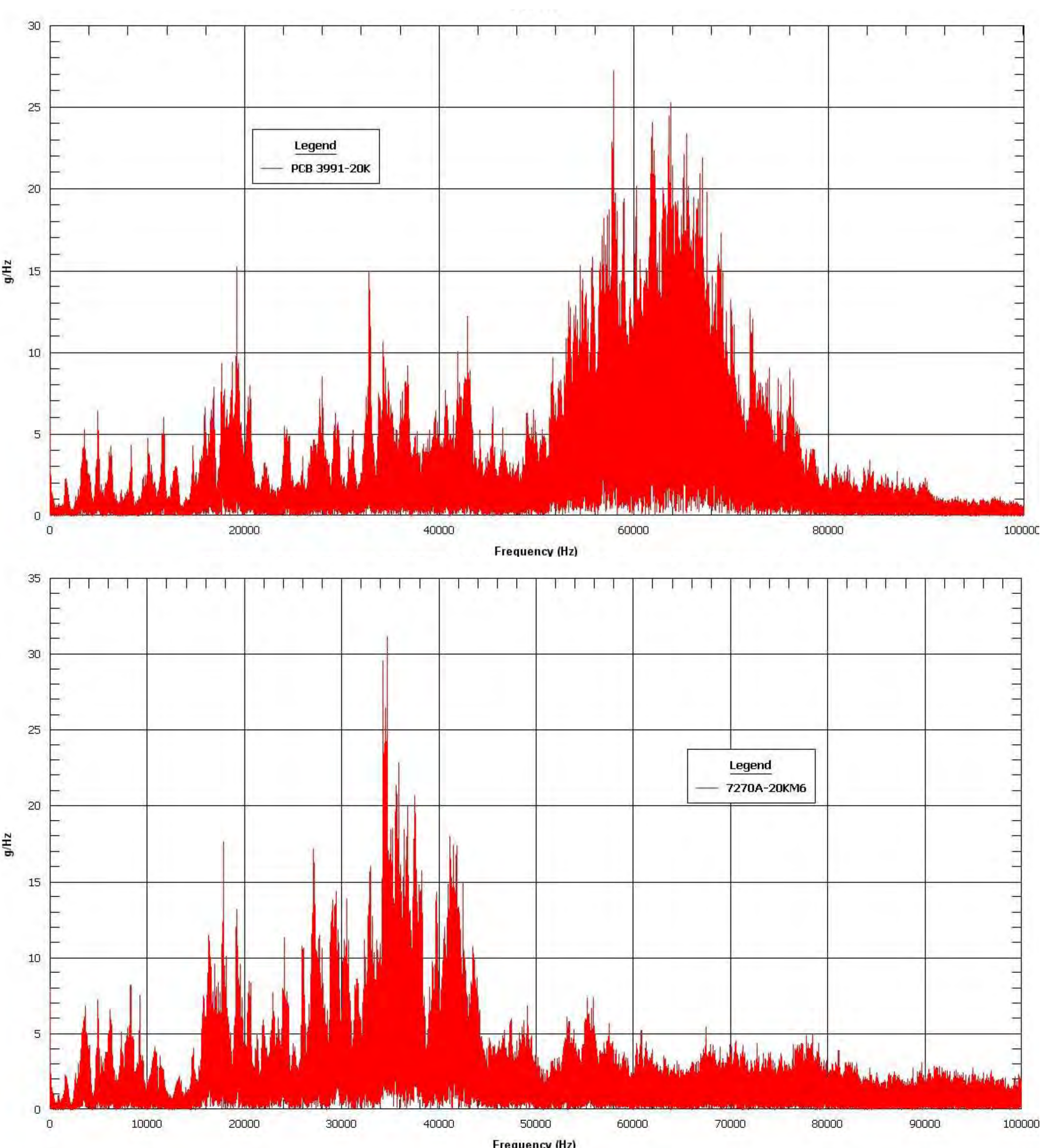

Figure 11. FFT of hammer tests, focusing below 100kHz. Above is the spectrum of the new sensor, showing the ~65kHz low Q resonance. Below is the 20kG legacy sensor, with ~30-40kHz low Q resonance in the housing of the mechanical filter. A similar plot was seen of the 60kG version. For all, the data below 25kHz matched fairly well. The next figure shows higher frequencies.

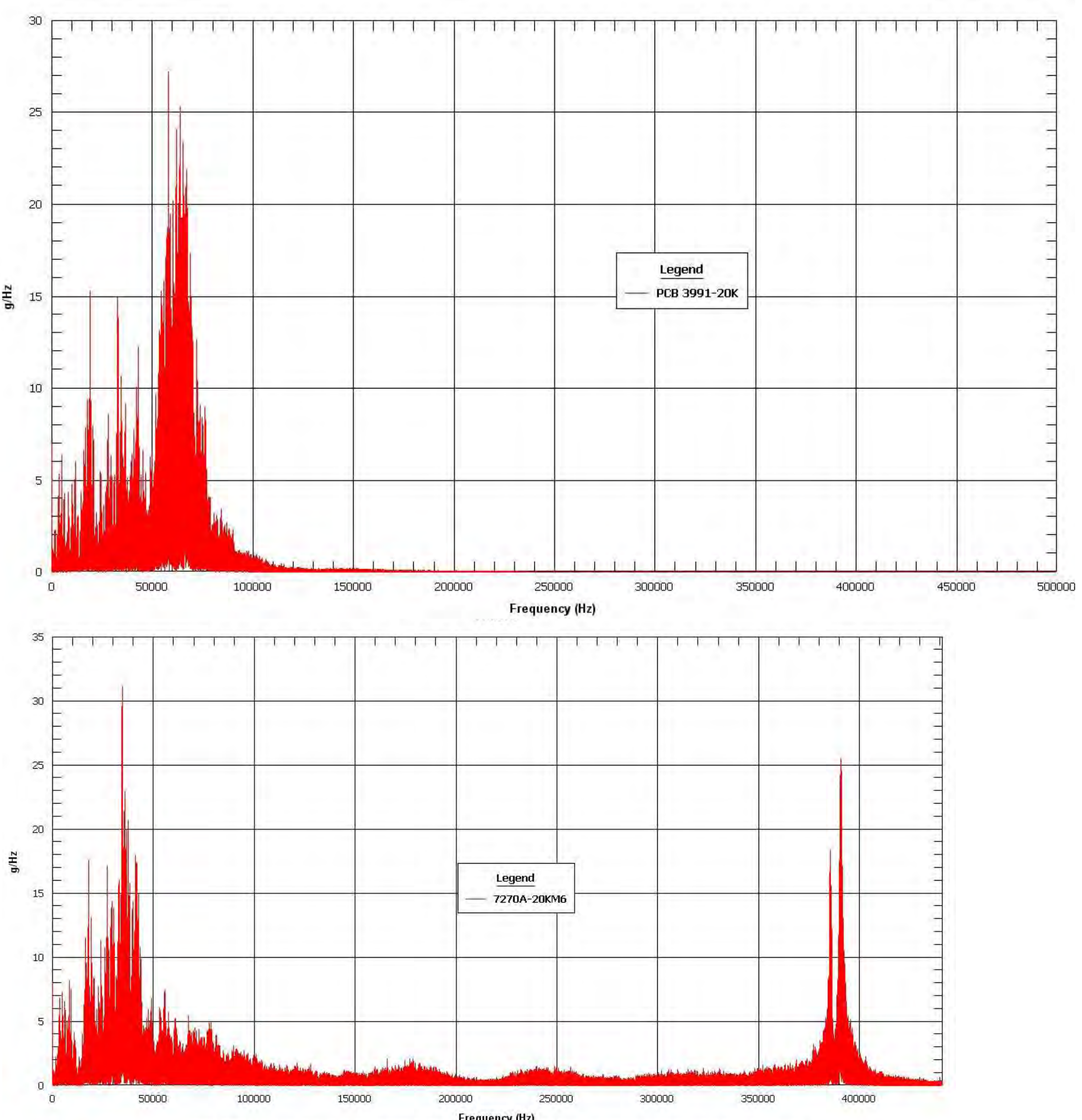

Figure 12. FFT of hammer tests through resonance. This is the same FFT results as in previous figure, but a wider view shows that the new sensor's low resonance and squeeze film damping effectively filtered higher frequency components, whereas the high Q 380kHz resonance of the 20kG legacy sensor comes through despite mechanical isolation. A similar plot of the 60kG legacy sensor showed a 900kHz resonance. A more revealing view of the high frequency components of the new sensor is shown in a logarithmic plot in Figure 14.

The preceding data shows that the damping of the new sensor provides effective protection yet delivers data uncorrupted by the mechanical filter used to keep the legacy sensor from resonating to failure. Understanding this damping was the subject of transient and shaker-based tests at the manufacturer, and is presented next.

Damping Tests

In the plot of Figure 13, the transient technique of logarithmic decrement δ was used to determine damping at resonance. The pertinent equations for the classic spring/mass/damper single degree of freedom system [3] are

- $\delta = \ln(x_1/x_2) = 2\pi\,\zeta\,/\,(\mathrm{sqrt}(1-\zeta^2)) = \zeta\,\omega_n\,\tau = \zeta\,n$
- $\zeta = c/c_c$, where c_c is critical damping
- for $x_1/x_2 = 2$, $\zeta = 0.11/n$
- $Q = 1/(2\zeta)$

The factor of 2 amplitude decay over a period τ is observed over 2.3 oscillations (**n**), and indicates damping of ζ = ~0.05 and Q = ~10.

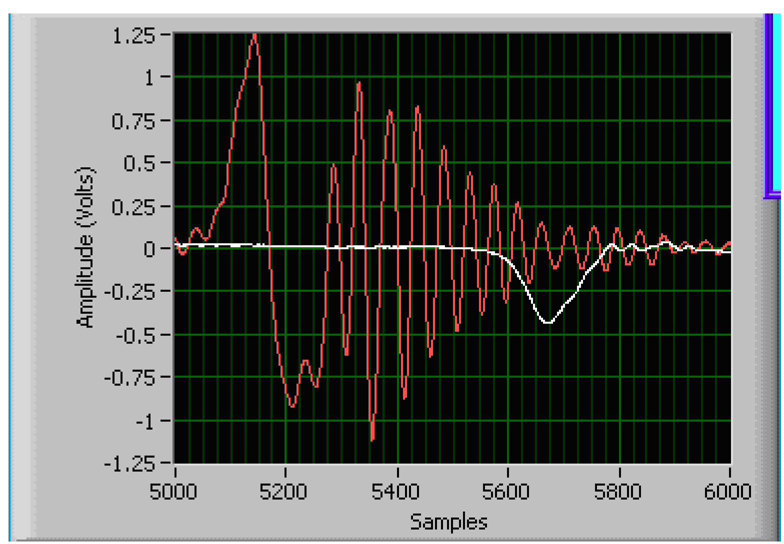

Figure 13. Logarithmic decrement of resonant response in the new sensor. Red trace is sensor resonance output with fast Hopkinson bar pulse, which decays 50% in a period of between 2 and 3 cycles. The white trace is strain gauge on bar. (Credit: T. Jaskolka of PCB Piezotronics Inc.)

Shock sensors in general have sensitivity so low that it is can be difficult to get reliable data from shaker-based sensitivity and phase frequency response data. A quadrature laser interferometer and a beryllium armature air bearing shaker is probably the most capable technique available and was utilized to get the sensitivity and phase data shown in Figure 14. (Credit: J. Dosch and J. Kessler of PCB Piezotronics Inc.)

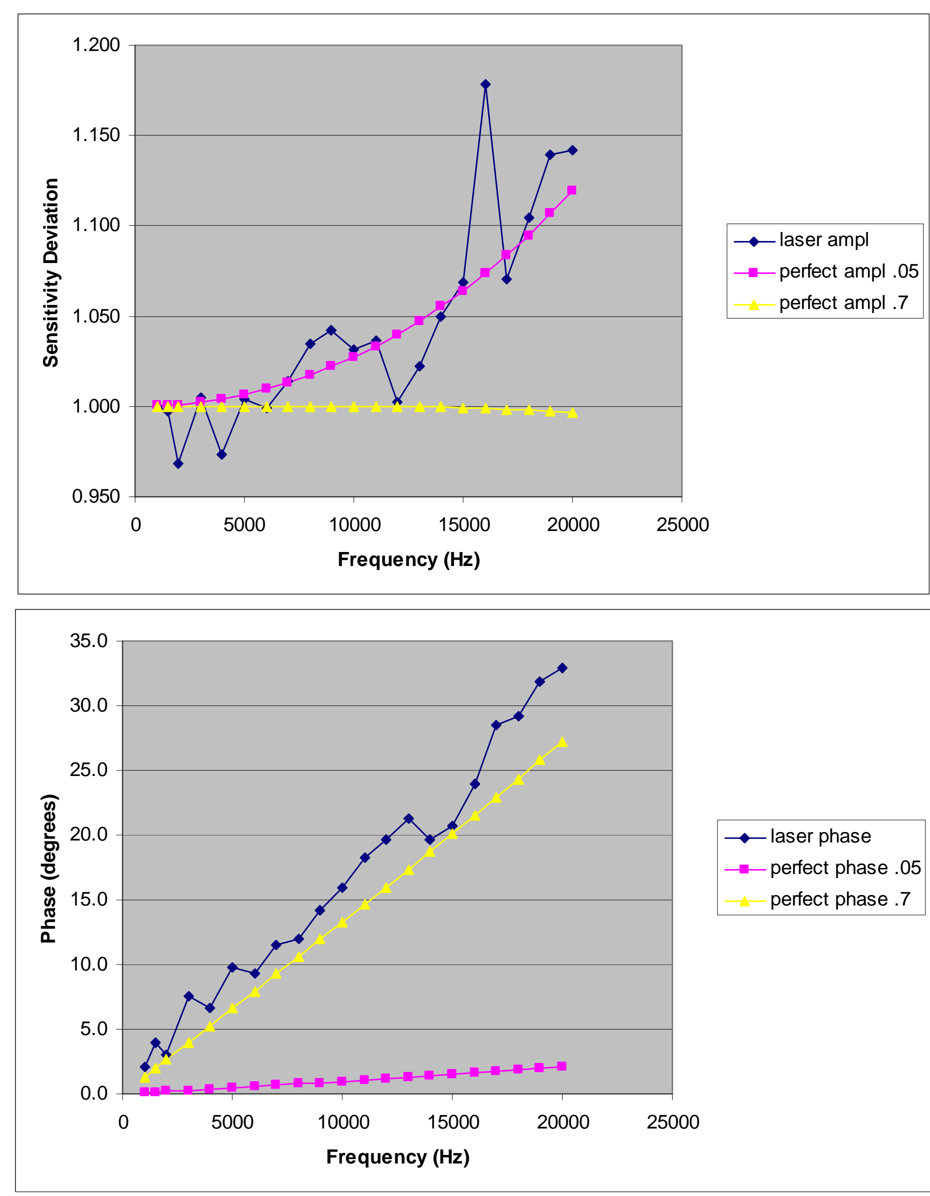

Figure 14. Shaker-based frequency response measurements, referenced to a laser interferometer. Data on sensitivity and phase for one sensor is shown in blue. Also shown are the theoretically perfect responses of a single degree of freedom system with resonance frequency of 61kHz, one with damping coefficient of 0.05 and another with optimally flat 0.7 damping. The sensitivity response at top matches the 5% damping curve, whereas the phase measurements at bottom closely match the "linear phase" of 70% damping. (The linear phase translates to a delay for all frequencies, meaning in this case that the entire waveform of a transient pulse would be shifted 4 microseconds. For comparison, in 4 microseconds the distance traveled by an object moving at Mach 1 would be 1.3 mm.)

This unusual dual nature of damping is probably explained by the non-linear and dual nature of squeeze film damping. That is, as frequency increases, forces involving air transition from being due to viscosity (from flow) to elasticity (from compression) of the air. Elastic forces don't dissipate energy, so damping decreases above ~10kHz and the effect of the resonance dominates the sensitivity curve. The damping at the resonance

frequency, as determined by transient technique of Figure 13, and as indicated in the hammer test redisplayed in Figure 15, also appears to match a low (~5%) value.

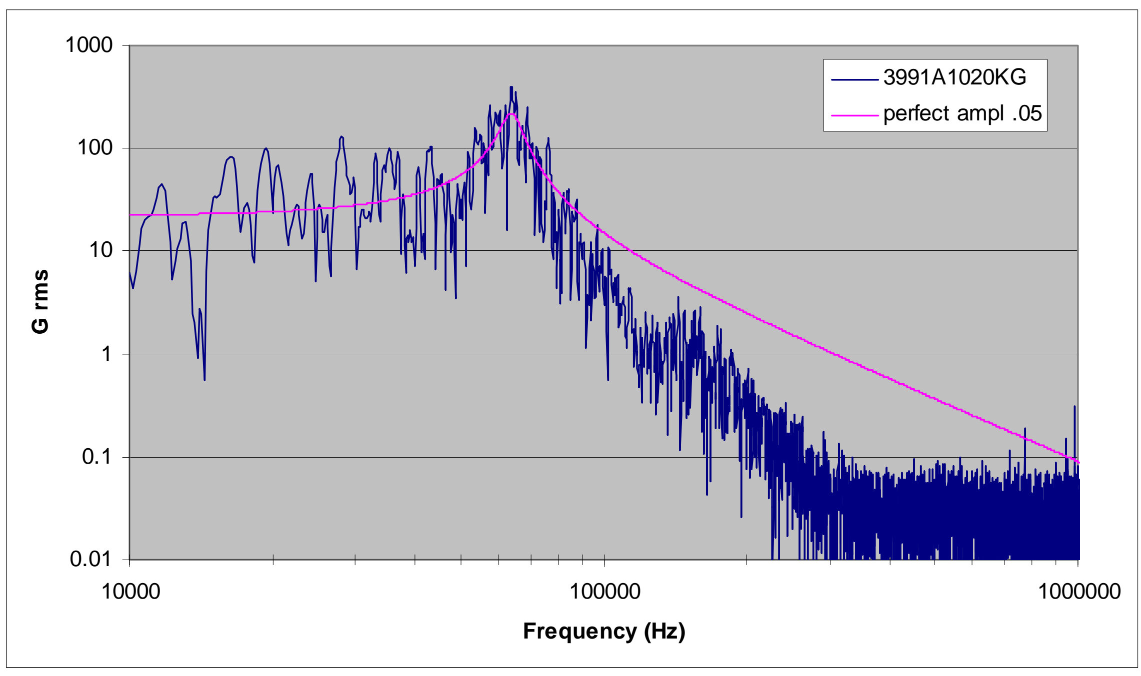

Figure 15. FFT of hammer response. Further analysis of the raw data of the new sensor from Figure 12, this time plotted on a logarithmic scale, indicates a damping coefficient of ~0.05 and no significant modes higher than the resonance.

Assuming that the energy is fairly white, that is, uniform over frequencies as indicated by the legacy sensor in Figure 11, the rolloff past the resonance in Figure 15 has a much steeper decline than a perfect single degree of freedom response to white noise, (which is what the curve labeled "perfect ampl .05" represents). This perhaps indicates that the squeeze film damping in the new sensor is more effective than expected. Such an efficient roll off of output by the sensor would make the requirements for sampling rates and antialiasing filters less demanding.

Failure Modes and Improvements

There were some failures of the new sensor, from two sources.

Electrostatic Discharge (ESD)

In normal handling over the first years of development, there had been no known instances of ESD damage, however failures occurred during extremely low humidity conditions in recent field tests. Microscopic inspection definitely identified the failure as ESD, and identified the easily-corrected root causes. The design and processes have been improved, and an additional mitigating design feature has been included into the next batch of sensors; but until then modest ESD precautions are advised to users of the new sensors.

Stress fracture

As mentioned previously, a 20kG device failed at >200kG on the Hopkinson bar facility shown in Figure 3. Failure analysis showed that only one of four cantilevers cracked, as shown in Figure 16, indicating a low-probability local condition rather than general failure. Internal stress concentrators have been identified and have been remedied in the next design revision.

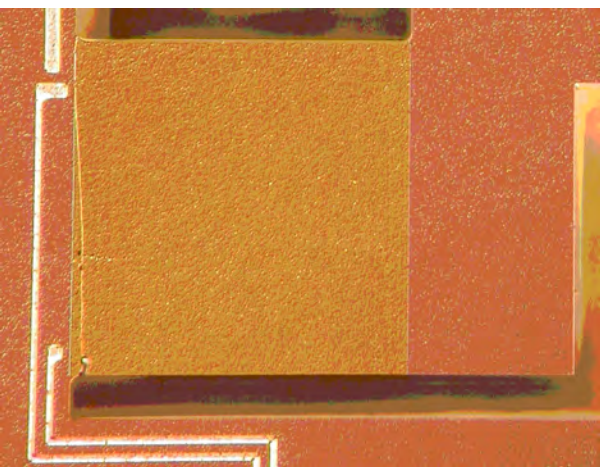

Figure 16. Overstress at >200kG. Theoretically the Over Range capability should be much higher, since the mechanical stops can take the additional load without subjecting the more flexible cantilevers to more stress.

Until the new Core wafers are completed and the improvements proven to increase the effectiveness of the stops, Over Travel stops will be set conservatively to ~30kG to avoid failure in extreme Over Range. Each of the devices currently manufactured in the conventional flat package has been fully tested at Over Range to three times Full Scale on a Hopkinson bar.

Although the 20kG sensor has been shown to handle most applications described, future applications may need unrestricted travel to above 30kG. With a simple modification to the design, the sensor family will be expanded to include a 60kG version. Sensor footprint is identical, so it will fit in all packages. It will have the same 200mV output (10V excitation) at 60kG Full Scale. Mechanical stops will be set at ~100kG. Resonance frequency is estimated to be at least ~100kHz, with frequency response flat to 5% to ~20kHz. Damping is predicted to be somewhat smaller the 20kG version, with smaller phase delay and a Q that will be slightly higher (~30) , but still significantly smaller than all versions of the legacy sensor (~1000).

Packaging Comparisons

The dynamics of shock accelerometer packages can have significant impact on fidelity of the reported shock. The conventional flat metal package has been used since the mid-1980's and was at the time an attempt to conform to the bolt pattern of an earlier model of the pre-MEMS era. Its design is not optimum. For instance, its bending flexibility has been known to cause failures in particularly large negative accelerations, in which the case momentarily leaves the surface and slaps down catastrophically. In addition, the

application of mounting torque can cause severe internal strain if the mounting surface is not flat, resulting in damage or shift in the ZMO. (Therefore, loss of preload of the screws during a shock can then appear as shock-induced zero shift.)

The following figures are intended to exhibit ideas for alternate packages to address these weaknesses in the legacy package. Further, the capability of a flip chip configuration in Figure 17 has the most revolutionary potential for miniaturization. Field evaluations will be required to prove out the effectiveness of these approaches, or expose weaknesses requiring further improvements.

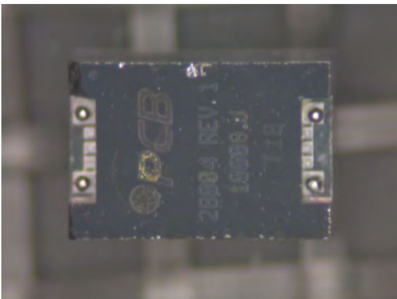

Figure 17. Proof-of-concept prototype of the "flip chip" configuration. The four larger aluminum pads are the wirebond pads which have been modified with solder "bumps" shown, so that solder balls can be attached for a "flip chip" configuration.

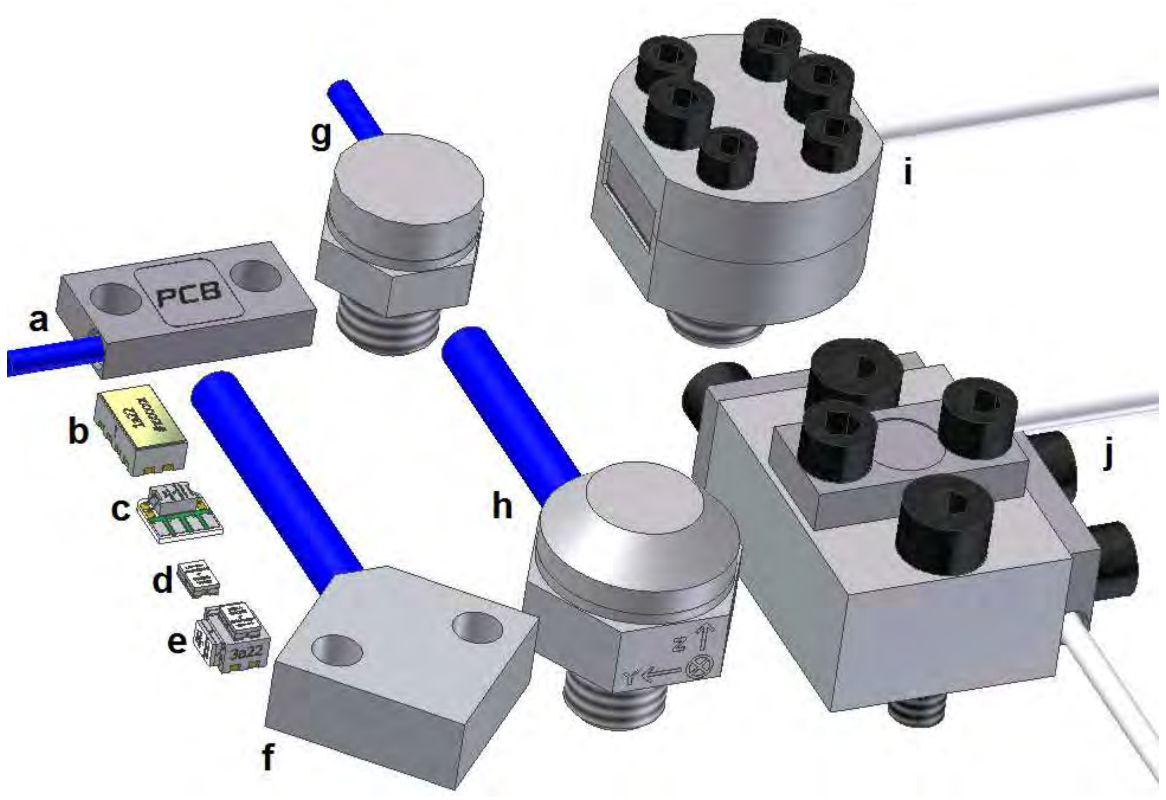

Figure 18. Packaging Comparisons. All are drawn to scale. The first three are current existing configurations: **a** is the conventional flat package, **b** is the surface mount package, and **c** is the substrate subassembly that is used inside of **a**, which can be used as a chip-and-wire configuration. In development currently, **d** is the flip chip version (a prototype of which was shown in Figure 17), and **e** is the surface mount triaxial block that connects three flip chip sensors to the circuit board. Once **e** is completed, it will be possible to make smaller versions of triaxial packages, such as **f**, which has the same hole pattern as the conventional package **a**, or a ¼-28 stud version in **h**. Such a robust package is also possible for the single axis in **g,** which should eliminate the effects of bending flexibility of the conventional flat package. Both **g** and **h** have the disadvantage that the orientation of the cable when fully screwed in is uncontrolled (dependent on the thread of the mounting hole). All of these configurations are small compared to the packages and fixtures of the legacy sensor shown in **i** (which is the mechanical filter featured in the hammer tests of Figures 8-12), and **j** (a triaxial block).

Conclusions

The new piezoresistive MEMS sensor was designed for severe applications such as concrete penetration and metal-on-metal or pyrotechnic impacts. The fundamental performance and survivability of the sensor was confirmed by the tests described. In these applications large high frequency components often mask the more important low frequency data (that is, those components with meaningful correlations to structural motion, which are often limited to below ~20kHz). In such applications it is vital to the measurement that there be insignificant zero shift. The tests performed confirmed this to be the case as well.

The sensitivity and range of the new sensor handled rigid body decelerations in simulated and real penetrations, and its resonance frequency and squeeze film damping was shown to provide meaningful data to high frequencies, and linear response to well above the full scale. Even when hard-mounted, the sensor internally filtered high frequency components which could cause potentially damaging resonant amplification of undamped sensors.

The design has been packaged for drop-in replacement to existing applications, but has the capability of being designed into other configurations such as flip chip mounting for extreme miniaturization and integration into circuit boards.

Because the resonance response of the new sensor has been suppressed by a low level of damping, resolution can be improved in systems which once used the extremely high Q legacy sensor. Whereas configurations for the legacy sensor required excessive "head room", using low gain of conditioning and data acquisition to accommodate resonant amplification, gain settings for the new sensor can be scaled to the measurement. Where the 60kG legacy version is replaced by the 20kG new sensor, an additional factor of three increase in output and therefore resolution will be attained. (A future new sensor with the same sensitivity at the 60kG legacy sensor, which will allow measurement to 100kG in the rare instances that is necessary, would also have damping, so the improved resolution through use of higher gain can still be attained.)

Finally, data acquisition for systems using the new sensor can be simplified, since the sample rate and electrical filter corners to avoid aliasing can be lowered by up to an order of magnitude. In addition, the high input impedance means power consumption by the new sensor is reduced an order of magnitude. Due to this and other design features, warm-up drifts are reduced, further simplifying system design.

Acknowledgments

The author wishes to acknowledge the skill of Andrea Tombros and An-Shyang Chu of PCB Piezotronics in converting a conceptual design into a functional silicon sensor.

References

[1] Sill, R., "Development of a Damped Piezoresistive MEMS High Shock Sensor", 78th Shock and Vibration Symposium, Nov 4-8, 2007, Philadelphia PA.

[2] white paper by Frew, D., and Duong, H., Sandia National Laboratories, "Performance Evaluation of PCB Model 3991High-G Accelerometer", Feb 5, 2008

[3] Thomson, W., Theory of Vibration with Applications, Prentice Hall, 1972, p29-30.

© 2021 PCB Piezotronics - all rights reserved. PCB Piezotronics is a wholly-owned subsidiary of Amphenol Corporation. Endevco is an assumed name of PCB Piezotronics of North Carolina, Inc., which is a wholly-owned subsidiary of PCB Piezotronics, Inc. Accumetrics, Inc. and The Modal Shop, Inc. are wholly-owned subsidiaries of PCB Piezotronics, Inc. IMI Sensors and Larson Davis are Divisions of PCB Piezotronics, Inc. Except for any third party marks for which attribution is provided herein, the company names and product names used in this document may be the registered trademarks or unregistered trademarks of PCB Piezotronics, Inc., PCB Piezotronics of North Carolina, Inc. (d/b/a Endevco), The Modal Shop, Inc. or Accumetrics, Inc. Detailed trademark ownership information is available at www.pcb.com/trademarkownership.

WPL_9_1121